Opto-Electronics Review 28 (2020) 164-170

PAN POLISH ACADEMY OF SCIENCES

Opto-Electronics Review

journal homepage: http://journals.pan.pl/opelre

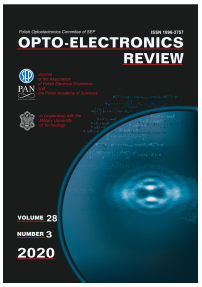

Performance analysis of an InAs/GaSb superlattice barrier photodetector covering the full LWIR spectral domain

R. Alchaar[a*], J.-B. Rodriguez[a], L. Höglund[b], S. Naureen[b], E. Costard[b], P. Christol[a]

[a] IES, Univ. Montpellier, CNRS, Montpellier, France
[b] IRnova AB, Electrum 236 - C5, SE-164 40 Kista, Sweden

Article info

Article history:
Received 28 May 2020
Accepted 17 Jun 2020

Keywords:
Barrier photodetector, InAs/GaSb type-2 superlattice, long wavelength infrared, performance analysis.

Abstract

In this paper, we present the electrical and electro-optical characterizations of an InAs/GaSb type-2 superlattice barrier photodetector operating in the full longwave infrared spectral domain. The fabricated detectors exhibited a 50% cut-off wavelength around 14 µm at 80 K and a quantum efficiency slightly above 20%. The dark current density was of 4.6×10^{-2} A/cm^2 at 80 K and a minority carrier lateral diffusion was evaluated through dark current measurements on different detector sizes. In addition, detector spectral response, its dark current-voltage characteristics and capacitance-voltage curve accompanied by electric field simulations were analyzed in order to determine the operating bias and the dark current regimes at different biases. Finally, dark current simulations were also performed to estimate a minority carrier lifetime by comparing experimental curves with simulated ones.

1. Introduction

For the infrared detector community, the longwave infrared (LWIR) atmospheric window is usually defined by wavelengths between 8 and 12 µm. However, a closer look reveals that the LWIR transparency window of the terrestrial atmosphere extends to 14 µm. This spectral region is suitable to detect thermal radiation intensities at room terrestrial temperatures or below in the upper atmosphere. Indeed, according to Wien's displacement law of thermal radiation, a blackbody at 300 K has a maximum photon emittance at 9.6 µm and this peak wavelength shifts to 14.5 µm for a temperature equal to 200 K. Consequently, it is relevant to consider the whole LWIR spectral domain between 8 and 14 µm to take advantage of the atmospheric transmittance window in this range for infrared (IR) imaging.

The main commercial high performance cooled detector systems currently available, made of quantum well infrared photodetectors (QWIP), mercury cadmium telluride (MCT) and type-II superlattice (T2SL) technologies, are mainly limited to the near LWIR domain, up to 10 µm [1-4]. However, considering an ideal blackbody at 300 K, without any IR system or transparency window considerations, the power emitted per unit area at the surface of the blackbody in the near LWIR range (8-10 µm) corresponds to only 35% of the total power emission in the full LWIR (8-14 µm) range. Therefore, taking into account the LWIR broadband spectral range would be useful for many applications including space-related ones.

Beyond 10 µm, the LWIR cooled detector technology is dominated by MCT operating at 80 K and extrinsic silicon blocked impurity band (BIB) detector, the latter operating at a very low temperature. Due to its high uniformity, bandgap adjustability by tuning the superlattice (SL) period thickness composition, low Auger recombination rate and high carrier effective mass, the InAs/GaSb T2SL detector can compete with well-established materials for the full LWIR spectral domain, up to 14 µm. Moreover, the InAs/GaSb T2SL can be implemented in a barrier structure, where a wide bandgap material is inserted between the absorbing layer and the contact layer with the objective of blocking majority carriers and allowing the flow of minority carriers. Compared to a standard LWIR photodiode, this configuration reduces the detector dark current by confining the electric field inside the barrier, thus greatly suppressing the generation-recombination (GR) current and achieving a diffusion limited performance at 80 K [5,6].

*Corresponding author: alchaar@ies.univ-montp2.fr

https://doi.org/10.24425/opelre.2020.134425

A few high-performance InAs/GaSb T2SL barrier detectors operating in the full LWIR domain with a cut-off higher than 12 µm have been reported with improving material growth quality and fabrication processes of pixel devices [7-10]. However, to date, no camera has been demonstrated and achieving such an imaging IR system will satisfy both terrestrial and extra-terrestrial applications [11,12].

In this paper, we report our latest work on the fabrication and characterization of an InAs/GaSb T2SL barrier detector device with a 50% cut-off wavelength near 14 µm at 80 K. Based on electrical and electro-optical measurements, a performance analysis was performed, as well as dark current simulations which allowed us to extract previously-unknown material parameters such as the minority carrier lifetime at this spectral range.

2. Structure description

The device reported here consists of a double heterostructure barrier design with a heavily n-type doped InAs/GaSb SL contact layer, an InAs/AlSb SL barrier and a lightly p-type doped 3.2 µm-thick InAs/GaSb SL absorber. The absorber composition was 17 MLs of InAs and 7 MLs of GaSb which should feature a cut-off wavelength of 14.5 µm at 80 K [13].

InAs/AlSb SL in the barrier is tailored to have a large offset in the valence band and minimal offset in the conduction band, therefore blocking majority holes and collecting photo-generated electrons. Figure 1 shows the band diagram of the previously described structure, simulated by using the software Silvaco ATLAS at 80 K, zero bias and nominal doping conditions [14].

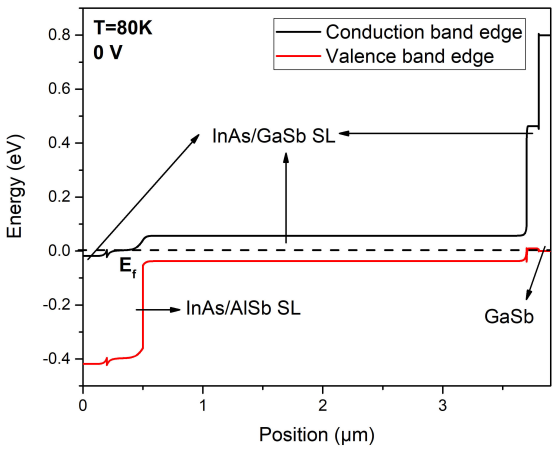

Fig. 1. Simulated band diagram of the barrier device structure at 80 K and zero bias. The black dashed line represents the Fermi level.

3. Fabrication and characterization

T2SL barrier structure was grown by a solid source molecular beam epitaxy (MBE) on an n-type GaSb substrates. Photoluminescence (PL) measurements were performed after having etched a sample down to the absorber. Figure 2 shows a PL measurement at 80 K with a peak position at 13.8 µm, fairly close to the targeted cut-off wavelength of 14.5 µm. Indeed, such energy difference that is no greater than 5 meV.

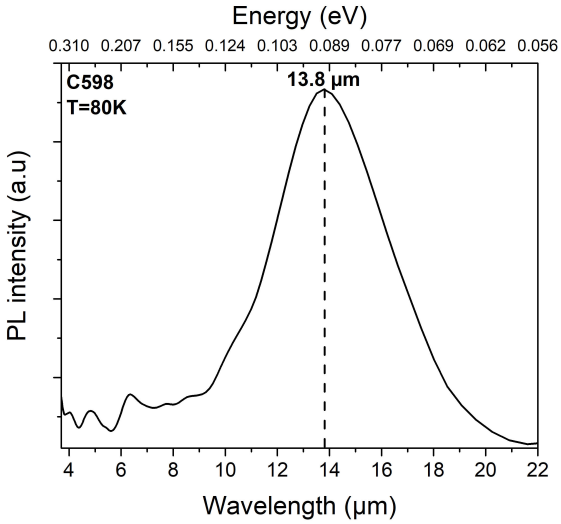

Fig. 2. PL measurement of the sample with a peak at 13.8 µm.

T2SL circular-mesa devices were then fabricated using a standard UV photolithography. Ti/Au were deposited as top and bottom contacts, as well as contact pads, by the electron beam evaporation. Shallow circular mesas were chemically etched using an acid-based solution [14]. Since the devices were shallow-etched, leakage current resulting from the etching process was suppressed and passivation was not required. A polymerized photoresist layer was used for the protection and electrical insulation of the mesas. Next, another chemical etching is carried out to reach the bottom contact layer. Figure 3 shows a photo of a shallow-etched mesa taken with a scanning electron microscope (SEM).

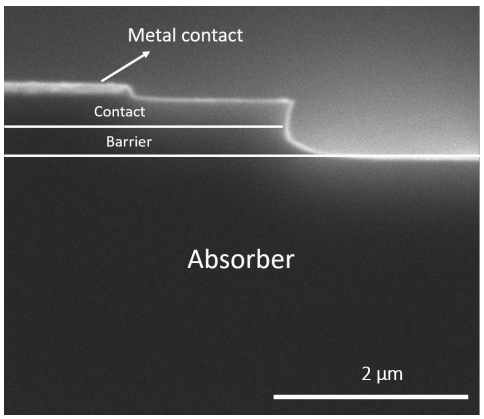

Fig. 3. Scanning electron microscope photo of a shallow-etched mesa.

The sample was placed inside a cryogenic probe station for electrical measurements. J(V) measurements were performed at 77 K on detectors with different sizes ranging from 60 to 210 µm and the results are shown in Fig. 4a). The curves are slightly dispersed with only a factor of 2 differences between the best and the worst current density measurement. The dark current density was extracted at -200 mV and plotted against the P/A ratio in Fig. 4b) and the resulting curve exhibits a minor size-dependence. Since the devices were shallow-etched, leakage current will be neglected and minority carrier lateral diffusion will be investigated instead, in order to explain the J(P/A) size

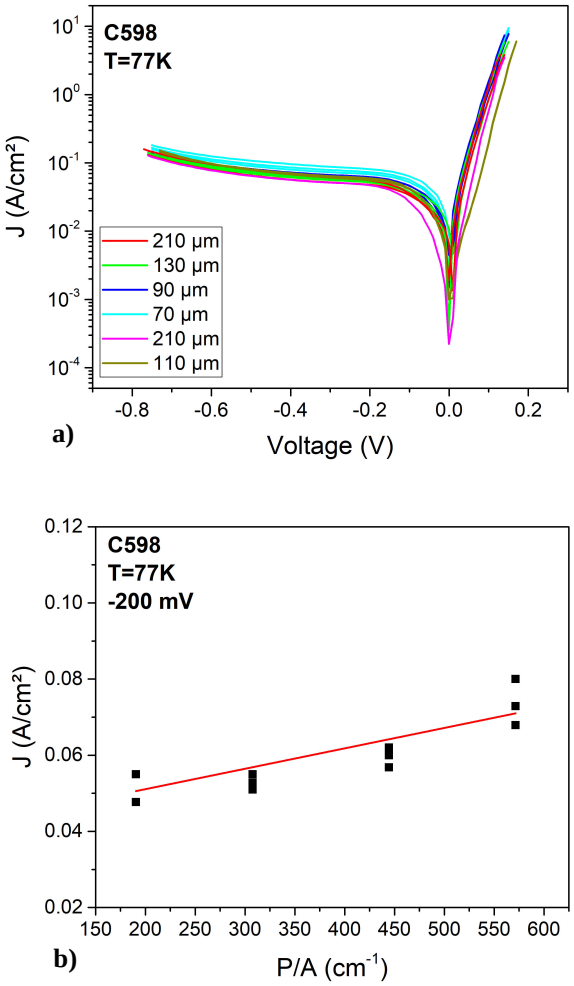

Fig. 4. Current density voltage measurements: a) performed on different detector sizes at 77 K. The detector diameters are shown in the legend; b) Current density as a function of P/A ratio, extracted at -200 mV.

dependence. In a shallow etch configuration, minority carriers can diffuse laterally to the electrical contacts from outside the etched mesa. Thus, the size of the device is defined by both the lateral diffusion length of electrons and the etched dimensions which may lead to an overestimation of the calculated dark current density. Lateral diffusion effects are more prevalent in small detectors, if their size becomes comparable to the diffusion length of minority carriers.

In order to estimate the lateral diffusion length, we have used the method described by Gopal [15] and used by Plis *et al.* [16] for InAs/GaSb T2SL-based detectors. If lateral diffusion is present, every mesa detector has the additional area A_t around the periphery of the detector which, in the case of circular mesas, can be expressed as:

$$A_t = \pi(r + L_e)^2 - \pi r^2, \tag{1}$$

where r is the etched mesa radius and L_e is the diffusion length of minority electrons.

As previously discussed, since the performance of smaller-area detectors is more dependent on lateral diffusion effects and less dependent on bulk effects than a larger-area detector, the diffusion length L_e in the limit $r \to 0$ can thereby be calculated as:

$$L_e = \sqrt{\frac{A_t}{\pi}}\,. \tag{2}$$

Equation (2) was used to evaluate the lateral diffusion length from Fig. 5a). First, current values were extracted at -200 mV for different mesa sizes and plotted *vs.* mesa area.

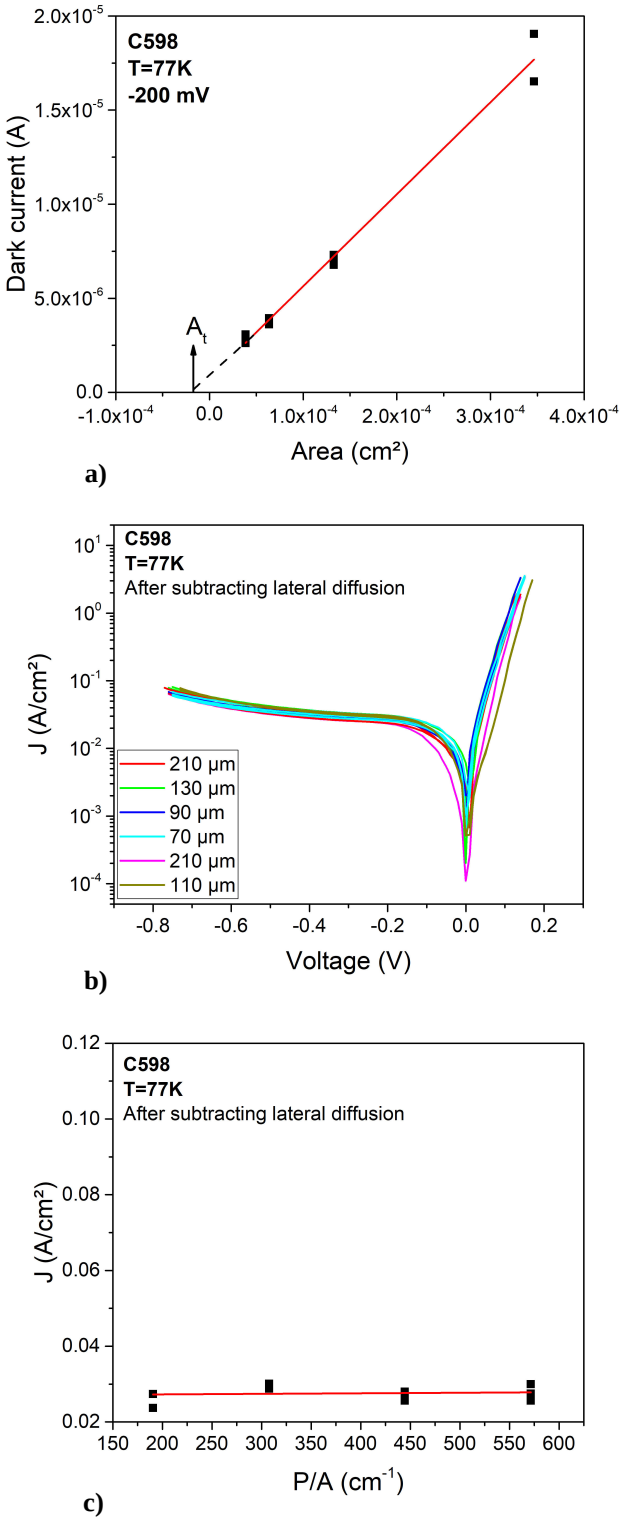

Fig. 5. In order to estimate the lateral diffusion length, a) dark current values were plotted, at -200 mV and 77 K, as a function of the mesa area to evaluate the lateral diffusion length. The red line represents the linear fit of the dark current which intersects at A_t with the x-axis; b) J(V) curves after subtracting lateral diffusion effects; c) Current density as a function of P/A after subtracting the lateral diffusion length.

A linear fit was performed and if the dark current is dominated by bulk processes, the fitting should intercept with the origin. When both bulk and lateral diffusion effects are present, the x-axis intercept of the fitting line corresponds to A_t. The deduced lateral diffusion length at 77 K was of 22 µm, comparable to values observed in previous studies [17]. The calculated lateral diffusion length is much larger than the growth-direction diffusion length which is expected to be in the order of the absorber thickness, i.e. ≈ 3.2 µm, highlighting the anisotropy of the LWIR InAs/GaSb T2SL. This anisotropy was studied theoretically [18], as well as experimentally [19] on MWIR InAs/GaSb T2SLs. In order to extend the cut-off wavelength of a T2SL detector, the period thickness is increased and as a result making the LWIR SL even more anisotropic as opposed to short-period SLs.

The dark current measurements from Fig. 4a) were then divided by a surface area that included the lateral diffusion length. The new dark current density curves are shown in Fig. 5b). After subtracting lateral diffusion effects, the curves are less dispersed than before and the resulting P/A curve in Fig. 5c) shows almost no size dependence, indicating a consistent electrical performance across the sample and that the approximation has been accurate.

Temperature-dependent measurements and the associated Arrhenius plot extracted at -200 mV are shown in Figs. 6a) and 6b), respectively. The activation energy was extracted by linearly fitting the curve in Fig. 6b) and its value was of 89 meV, equal to the measured bandgap energy at 80 K indicating a diffusion-limited performance. The photocurrent dominates the measured current density at 60 K and below, illustrated by the temperature-independent current density in this temperature range.

The photoresponse (PR) and quantum efficiency (QE) spectra of the devices were also measured. The bias-dependent normalized photoresponse signal in Fig. 7 increases with increasing reverse bias and starts to saturate at ~ -200 mV. The curve in the inset of Fig. 7 shows a peak QE (measured at $\lambda \approx 10$ µm) slightly above 20%, with no anti-reflection coating applied, in line with already published results for similar detector systems [7,20,21].

4. Performance analysis

In an effort to determine the turn-on, operating, generation-recombination (GR) and tunneling biases, we will follow the same analysis reported in Refs. 14 and 22. Normalized PR values at different biases were extracted from Fig. 7, the dark current density and its associated R_dA product from Fig. 6a) and, finally, an $(A/C)^2$ curve, from a capacitance-voltage measurement were plotted as a function of the voltage, at 80 K in Fig. 8 in order to identify the different dark current regimes. The first significant bias value, V_{on} (turn-on bias) is located at the first R_dA minimum at -80 mV. Then, the R_dA peak at -250 mV corresponds to the operating bias V_{op}. The photoresponse is maximized and the device is fully turned on at this bias. Furthermore, a slope change can be observed in the $(A/C)^2$ curve at this bias, signifying the full depletion of the barrier. At -370 mV, which was defined as V_{GR}, the diffusion plateau ends and GR current dominates indicating the beginning of the absorber depletion. Finally, tunneling

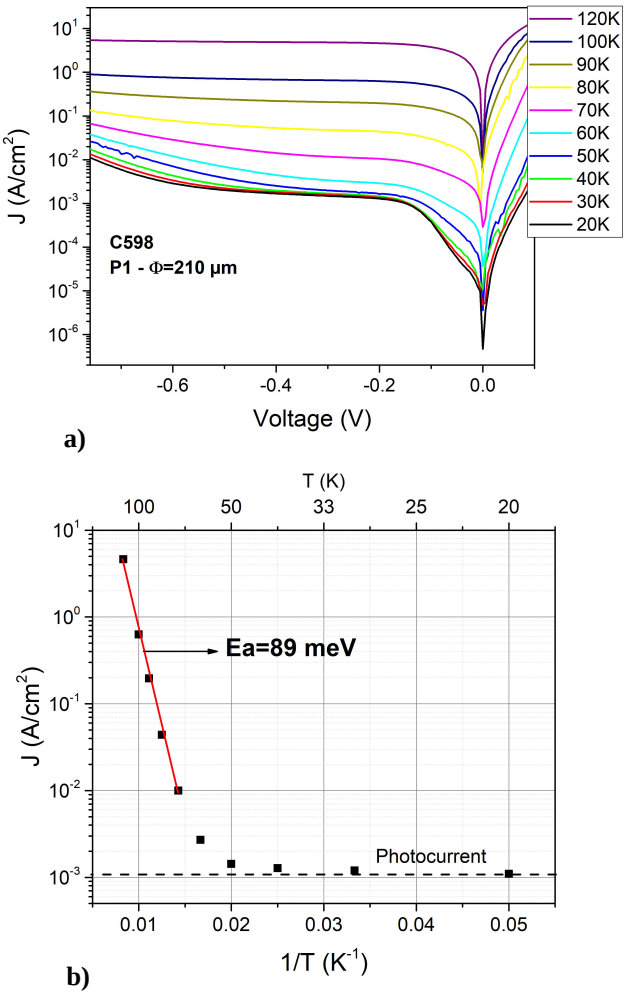

Fig. 6. Current density plots showing a) temperature-dependent measurements performed on a 210 µm-diameter detector; b) Arrhenius plot extracted at -200 mV. The red line represents the fitting for activation energy estimation and the dashed line is the photonic current limit.

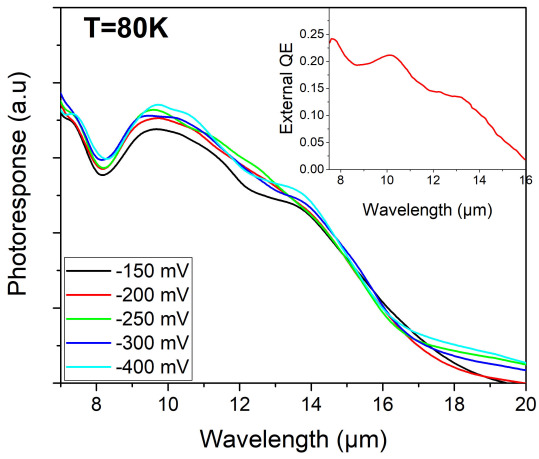

Fig. 7. Bias-dependent photoresponse measurements at 80 K. The inset shows the quantum efficiency at 80 K and -250 mV.

dominates the measured dark current density at -600 mV and onward. The dark current density at 80 K and V_{op} was of 4.65×10^{-2} A/cm^2 and R_dA was of 34 Ω·cm^2. It is then safe to assume that the electric field is confined inside the barrier between 0 V and V_{GR}. As a result, the extracted

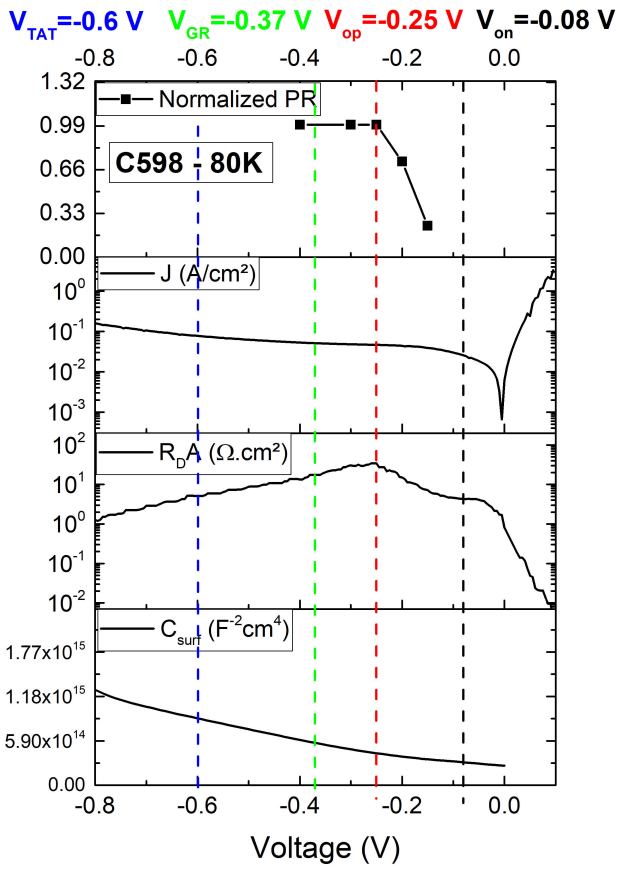

Fig. 8. Compiled electrical and electro-optical characterizations performed on the T2SL full LWIR barrier detector. The stacking of the curves allows to identify different dark current regimes occurring in the detector.

doping between 0 and V_{GR} corresponds to the barrier and the extracted doping after V_{GR} belongs to the absorber. The doping levels were of 1.5×10^{16} and 6.5×10^{15} cm^{-3} for the barrier and absorber, respectively, close to the targeted values (2×10^{16} cm^{-3}). Doping was extracted using the following equation:

$$\left(\frac{A}{C}\right)^2 = \frac{2}{q\epsilon_0\epsilon_{SL}}\left(\frac{V_d - V}{N_{dop}}\right), \quad (3)$$

where ϵ_0 is the vacuum permittivity, ϵ_{SL} is the permittivity of the SL (taken as the weighted average of the SL period: 15.3 for the InAs/GaSb SL and 14.8 for the InAs/AlSb SL), V is the applied bias, V_d is the diffusion potential in the junction, and N_{dop} is the net doping concentration.

It should also be noted that the observed operating bias value (-250 mV) is higher than anticipated. This minor inconvenience could be a result from a misalignment between the absorber and barrier layers, impeding the flow of minority carriers, that require a higher reverse bias to overcome the offset induced by this misalignment. For that, a design optimization is required, in order to lower the operating bias as much as possible, by adjusting the layer alignment between the absorber and barrier layers.

In order to complete the above analysis, the band diagrams and electric field were simulated as well at 80 K. Each simulation was performed at one of the biases reported in Fig. 8 and the results are shown in Fig. 9.

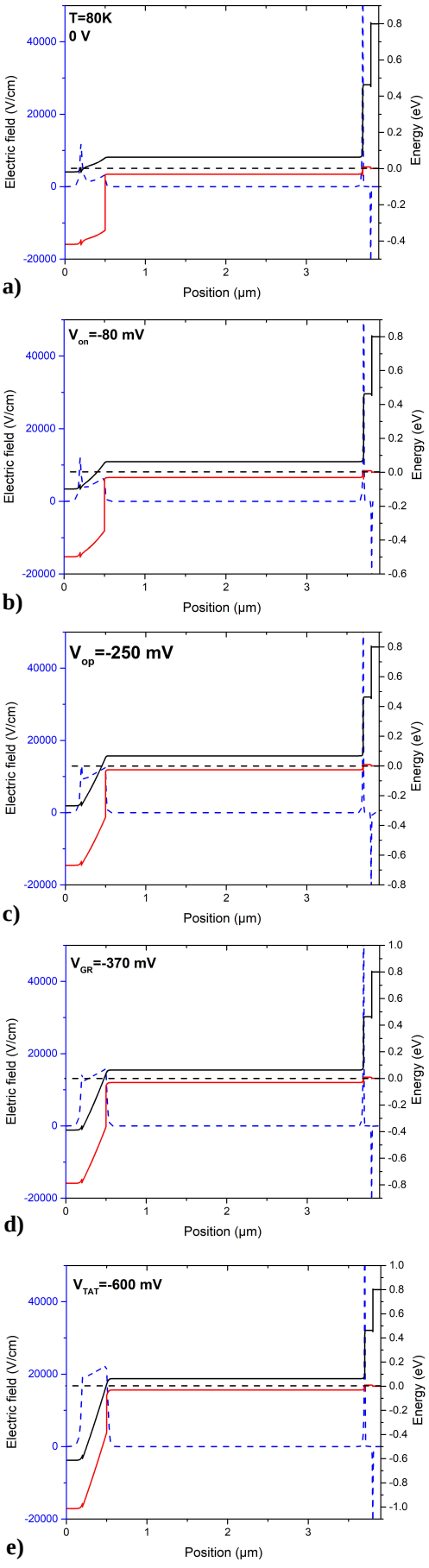

Fig. 9. Simulated band diagrams and electric field (blue dashed line) at a) 0 V; b) V_{on}; c) V_{op}; d) V_{GR}, and e) V_{TAT}, all performed at 80 K. The black dashed line represents the Fermi level.

Between 0 V and V_{GR}, the electric field is entirely confined inside the barrier. With an increasing reverse bias to V_{GR}, a full barrier depletion occurs resulting in the start of the domination of the GR current. Reaching V_{TAT}, the absorber is increasingly depleted and the tunneling regime takes over the dark current. The aim of these simulations is to complement the performance analysis, by visualizing the electric field evolution in the structure at different biases.

5. Minority carrier lifetime extraction

Dark current simulations were performed at several temperatures and subsequently compared to experimental curves. This would later help us to estimate experimentally unknown material parameters. The Silvaco ATLAS simulation model is detailed in our previous work [14]. Doping concentrations acquired from C-V measurements were utilized in the simulations, as well as the bandgap energy obtained from PL. Electron and hole effective masses were required to calculate the density of states and were taken from Ref. 14. The Varshni parameters (α and β), required for temperature-dependent bandgap simulations, were extracted from temperature-dependent photoluminescence measurements. The rest of the parameters required for the simulation were either experimentally-unknown or user-defined, such as the carrier lifetime ($\tau_{n,p}$), the tunneling effective mass (m_t) and the trap energy level inside the bandgap (E_t), i.e., the energy difference between the trap level and the intrinsic Fermi level. These parameters were adjusted until an agreement between simulated and experimental curves was achieved. The experimental and simulated J-V curves, in the temperature range of 80 K-120 K, are shown in Fig. 10a). A good agreement between simulation and experiment can be observed, indicating an accurate model and material parameters which were summarized in Table 1.

Table 1
InAs/GaSb SL material parameters extracted from simulations or experimentally measured.

Carrier lifetime at 80 K (ns)	19
Electron effective mass ($\times m_0$)	0.04
Hole effective mass ($\times m_0$)	0.75
Permittivity	15.3
Measured bandgap energy at 80 K (eV)	0.0898
Calculated Varshni parameters: α (eV/K)	1.678×10^{-4}
β (K)	270
Trap energy level E_t (eV)	0.008
Tunneling effective mass m_t ($\times m_0$)	0.023

The minority carrier lifetime was adjusted to fit the measurement for each temperature and Figure 10b) shows the estimated carrier lifetime at each temperature. A fitting was applied to the curve demonstrating that the lifetime follows a $T^{-1/2}$ trend which indicates a Shockley-Read-Hall (SRH)-limited lifetime in this temperature range [23]. The estimated lifetime at 80 K was of 19 ns, understandably shorter than measured values for InAs/GaSb T2SLs having a shorter LWIR cut-off wavelength [24]. Extending the detector cut-off

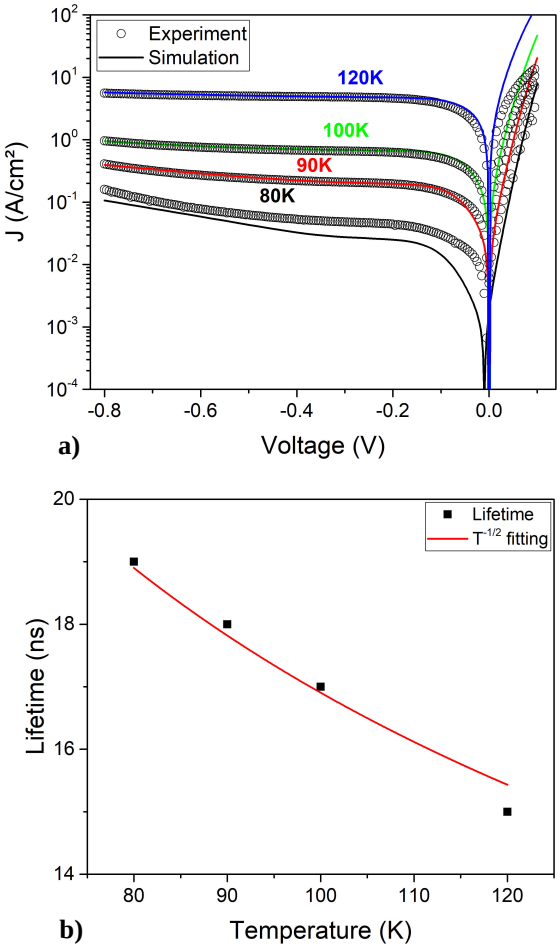

Fig. 10. Dark current simulations were used to a) compare measured and simulated current density curves at different temperatures and b) extract minority carrier lifetimes from the simulations at different temperatures. The red line represents the $\tau \propto T^{-1/2}$ curve fitting.

wavelength to cover the full LWIR spectrum results in a narrower bandgap and an increased non-radiative carrier generation-recombination rate which, in turn, results in a shorter carrier lifetime. Consequently, the short SRH-dominated carrier lifetime observed in InAs/GaSb T2SLs results in dark current values as high as one order of magnitude above the MCT benchmark "Rule 07" [25,26].

6. Conclusions

In conclusion, we have reported the characterization and performance analysis of an infrared barrier detector based on InAs/GaSb T2SL operating in the full LWIR spectral domain. Detector exhibited a cut-off wavelength near 14 µm at 80 K, confirmed by a photoluminescence measurement, with a dark current density of 4.6×10^{-2} A/cm^2 diffusion-limited down to 80 K and QE of 20% at 10 µm. Photoresponse, dark current, differential resistance, capacitance-voltage measurements with the help of electric field simulations were employed to identify different current mechanisms and significant bias values, such as the operating bias which was of -250 mV. Modelling the different dark current contributions allowed us to extract a carrier lifetime value of 19 ns from experimental curves at 80 K. The fabrication and characterization of full LWIR focal plane arrays will be the subject of forthcoming investigations.

Authors' statement

Research concept and design, R.A.; J.-B.R.; L.H.; S.N.; E.C. and P.C.; collection and/or assembly of data, R.A.; data analysis and interpretation, R.A.; J.-B.R.; L.H.; S.N.; E.C. and P.C.; writing the article, R.A.; critical revision of the article, R.A.; J.-B.R.; P.C.; L.H.; S.N. and E.C.; final approval of article, P.C. and R.A..

Acknowledgements

This work was partially funded by the French "Investment for the Future" program (EquipEx EXTRA, ANR 11-EQPX-0016) and ESA contract 4000116260/16/ NL/BJ.

References

[1] Klipstein, P. C. *et al.* Type II superlattice technology for LWIR detectors. in *Proc.SPIE* vol. 9819 (2016).

[2] Gunapala, S. D. et al. Large area III–V infrared focal planes. Infrared Phys. Technol. 54, 155–163 (2011).

[3] Rubaldo, L. *et al*. Latest improvements on long wave p on n HgCdTe technology at Sofradir. in *Proc.SPIE* vol. 10177 (2017).

[4] Rogalski, A., Martyniuk, P. & Kopytko, M. Type-II superlattice photodetectors versus HgCdTe photodiodes. *Prog. Quant. Electron.* **68** 100228 (2019).

[5] Klipstein, P. XBnn and XBpp infrared detectors. *J Cryst. Growth* **425**, 351-356 (2015).

[6] Delmas, M., Rossignol, R., Rodriguez, J. & Christol, P. Design of InAs/GaSb superlattice infrared barrier detectors. *Superlattice. Microst.* **104**, 402-414 (2017).

[7] Nguyen, B.-M., Bogdanov, S., Pour, S. A. & Razeghi, M. Minority electron unipolar photodetectors based on type II InAs/GaSb/AlSb superlattices for very long wavelength infrared detection. *Appl. Phys. Lett.* **95**, 183502 (2009).

[8] Jiang, D. *et al.* Very high quantum efficiency in InAs/GaSb superlattice for very long wavelength detection with cutoff of 21 μm. *Appl. Phys. Lett.* **108**, 121110 (2016).

[9] Li, X., Jiang, D., Zhang, Y. & Zhao, L. Interface optimization and fabrication of InAs/GaSb type II superlattice for very long wavelength infrared photodetectors. *Superlattice. Microst.* **91**, 238-243 (2016).

[10] Katayama, H. *et al.* Development status of Type II superlattice infrared detector in JAXA. in *Proc.SPIE* vol. 8704 (2013).

[11] Minoglou, K. *et al.* Infrared image sensor developments supported by the European Space Agency. *Infrared Phys. Techn.* **96**, 351-360 (2019).

[12] Sakai, M. *et al.* Development of Type-II superlattice VLWIR detectors in JAXA. in *Proc.SPIE* vol. 10177 (2017).

[13] Ting, D. Z., Soibel, A., Khoshakhlagh, A., Höglund, L., Keo, S. A., Rafol, B., Hill, C. J., Fisher, A. M., Luong, E. M. & Nguyen, J. in *Proc. SPIE.* 101770N.

[14] Alchaar, R., Rodriguez, J.-B., Höglund, L., Naureen, S. & Christol, P. Characterization of an InAs/GaSb type-II superlattice barrier photodetector operating in the LWIR domain. *AIP Advances* **9**, 055012 (2019).

[15] Gopal, V. Variable-area diode data analysis of surface and bulk effects in HgCdTe photodetector arrays. *Semicond. Sci. Tech.* **9**, 2267 (1994).

[16] Plis, E. *et al.* Lateral diffusion of minority carriers in n Bn based type-II InAs/GaSb strained layer superlattice detectors. *Appl. Phys. Lett.* **93**, 123507 (2008).

[17] Höglund, L. *et al*. Influence of shallow versus deep etching on dark current and quantum efficiency in InAs/GaSb superlattice photodetectors and focal plane arrays for long wavelength infrared detection. *Infrared Phys. Technol.* **95**, 158–163 (2018).

[18] Klipstein, P. *et al*. Minority carrier lifetime and diffusion length in type II superlattice barrier devices. *Infrared Phys. Techn.* **96**, 155-162 (2019).

[19] Suchalkin, S.*et al.* In-plane and growth direction electron cyclotron effective mass in short period InAs/GaSb semiconductor superlattices. *J Appl. Phys.* **110**, 043720 (2011).

[20] Han, X. *et al*. Very long wavelength infrared focal plane arrays with 50% cutoff wavelength based on type-II InAs/GaSb superlattice. *Chinese Phys. B* **26**, 018505 (2017).

[21] Wei, Y. *et al.* High Structural Quality of Type II InAs/GaSb Superlattices for Very Long Wavelength Infrared Detection by Interface Control. *IEEE J. Quantum Electron.* **48**, 512–515 (2012).

[22] Durlin, Q. *et al.* Midwave infrared barrier detector based on Ga-free InAs/InAsSb type-II superlattice grown by molecular beam epitaxy on Si substrate. *Infrared Phys. Techn.* **96**, 39-43 (2019).

[23] Connelly, B. C., Metcalfe, G. D., Shen, H. & Wraback, M. Direct minority carrier lifetime measurements and recombination mechanisms in long-wave infrared type II superlattices using time-resolved photoluminescence. *Appl. Phys. Lett.* **97**, 251117 (2010).

[24] Donetsky, D., Belenky, G., Svensson, S. & Suchalkin, S. Minority carrier lifetime in type-2 InAs–GaSb strained-layer superlattices and bulk HgCdTe materials. *Appl. Phys. Lett.* **97**, 052108 (2010).

[25] Rhiger, D. R. Performance comparison of long-wavelength infrared type II superlattice devices with HgCdTe. *J Electron. Mater.* **40**, 1815-1822 (2011).

[26] Rogalski, A., Martyniuk, P. & Kopytko, M. InAs/GaSb type-II superlattice infrared detectors: Future prospect. *Appl. Phys. Rev.* **4**, 031304 (2017).